



REGULAR PAPER

Numerical simulation of the pressure characteristics of the pulsed jet actuator

T. Zhu[†] , Y. Pan and J. Morrison 

Department of Aeronautics, Imperial College London, London, UK

Corresponding author: T. Zhu; Email: taihang.zhu17@imperial.ac.uk

Received: 8 June 2023; Revised: 30 August 2023; Accepted: 5 September 2023

Keywords: pulsed jet; numerical simulation; dynamic mode decomposition

Abstract

A compressible large eddy simulation (LES) is performed to study a pulsed jet actuator that is used to control a turbulent axisymmetric bluff body wake. The actuator is driven at low-frequency ($f = 200\text{Hz}$, $St_\theta = 0.029$) and high amplitude ($C_\mu = 0.034$). The numerical scheme and a suitable boundary condition for the pulsed jet are validated, showing good agreement with experimental results. A comparison of the velocity boundary condition and the moving boundary condition shows that, in the vicinity of the orifice/slot and in the downstream region, the results from these two methods are identical, while the fluid behaviour inside the cavity shows difference. An analysis of the pulsed jet actuator shows that the phase lag of the cavity pressure is determined by the integration of the diaphragm motion and the pulsed jet. The mean total pressure distribution shows that the total pressure loss is concentrated in the vicinity of the slot. Dynamic mode decomposition (DMD) on the pressure field is used to extract coherent structures which oscillate with the same frequency as that of the diaphragm motion. Some small-scale high-frequency structures are also apparent.

Nomenclature

A	area
C_p	pressure coefficient
$\overline{C_p}$	time averaged pressure coefficient
C'_p	turbulent pressure coefficient
C_{pT}	total pressure coefficient
$\langle C_p \rangle$	area-weighted averaged pressure coefficient
C_μ	blowing coefficient
D	diameter
DMD	dynamic mode decomposition
f	frequency
Re	Reynolds number
LES	large eddy simulation
L_s	slot length
St	Strouhal number
t	time
$\hat{u}, \hat{v}, \hat{w}$	velocity components
U, V, W	time averaged velocity components
u, v, w	turbulent velocity components

[†]Current affiliation at Shanghai Automotive Wind Tunnel Center, Tongji University and School of Automotive Studies, Tongji University and Shanghai Key Lab of Vehicle Aerodynamics and Vehicle Thermal Management Systems.

Greek symbol

ϕ	phase
ρ	density
θ	boundary layer momentum thickness

1.0 Introduction

The pulsed jet (synthetic jet, or zero-net-mass-flux jet) is generated by the periodic ingestion and expulsion of the working fluid through a slot or orifice [1]. Without any external flow source, the pulsed jet is able to transfer momentum to the flow system with a wide range of frequency and amplitude [2]. Therefore, it is widely used in aerodynamic flow control, especially in controlling bluff body wakes, where the pressure drag can be reduced by pulsed jet forcing. For instance, by applying a high-frequency periodic pulsed jet in the vicinity of an axisymmetric bluff body trailing edge, a base pressure recovery of 33% is achieved by Oxlade et al. [3]. The forced wake is modelled with a weakly nonlinear model by Rigas et al. [4]. Cabitza [5] applied the pulsed jet to a rectangular-sectioned bluff body and achieved a base pressure recovery of 27%. Barros et al. [6] applied a positive flux pulsed jet together with the Coanda effect to a similar geometry and achieved a drag reduction of 20%. The mechanism behind this phenomenon was analysed by Haffner et al. [7], and the effect of asymmetric forcing is also investigated [8]. The research by Pastoor et al. [9] shows that a 40% increase in base pressure is achievable by applying a low-frequency pulsed jet to a D-shaped bluff body. The pulsed jet is also used to vary the aerodynamic loads of a freely yawing axisymmetric bluff body by controlling the wake symmetry [10, 11].

While the pulsed jet has been successfully applied experimentally for controlling the bluff body wake, few numerical studies have been conducted to study the pulsed jet actuator. In previous work [12–15], simulations of the actuator cavity and diaphragm are often omitted and the pulsed jet is prescribed as a velocity boundary condition. This type of method benefits from lower computational cost since the diaphragm, the cavity and the slot are omitted, while some characteristics of the pulsed jet, such as the fluid motion inside the slot and cavity and the pressure character, are not fully understood: while the actuators are usually of zero net mass flux design, the momentum flux is necessarily non-zero.

The boundary condition of the actuator is important for the numerical simulation of the pulsed jet [16, 17]. Two techniques have been used: the moving boundary condition, where the volume of the cavity is changed by boundary deformation, or the velocity boundary condition, where a velocity transpiration boundary condition is applied to the diaphragm to compress or decompress the fluid without changing the volume of the cavity. Some comparative studies have been conducted to achieve an optimal simulation method. However, the conclusions are not consistent: the 2D compressible simulation result by Yoo et al. [18] and Jain et al. [19] demonstrates that there are obvious differences between the velocity boundary condition result and the moving boundary condition one. The 3D numerical result by Bazzidi-Tehrani et al. [20] shows that these two methods achieve an almost identical result with an incompressible solver, while compressibility may introduce a noticeable difference. The incompressible simulation conducted by Ma et al. [21] indicates that difference is only slight: the downstream velocity structure is identical but slightly different inside the cavity. Since these conclusions are inconsistent, both the moving boundary condition [22] and the velocity boundary condition are developed here to verify these two methods and to validate the LES numerical scheme.

In the present study, we provide a further understanding of the flow inside and outside the actuator and build a basis for further numerical simulation of the pulsed jet forced wake [23]. The actuator boundary condition is compared to the experimental work by Feero et al. [24]. In particular, the total pressure losses near the actuator slot are assessed. The DMD is used to analyse the pressure field in the downstream region and on the base.

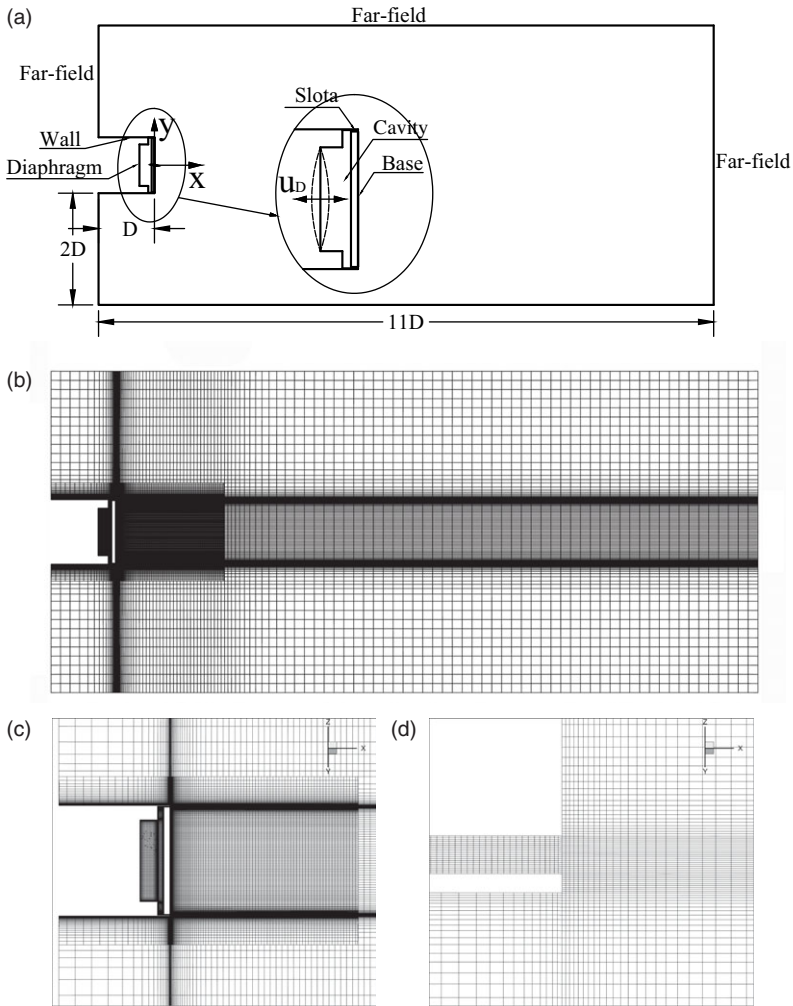


Figure 1. (a) The computational domain, (b) the mesh for the numerical simulation (c) and (d) show amplified views of the wake area and the jet slot, respectively.

2.0 Numerical methodology

2.1 Geometry definition and numerical scheme

Figure 1 shows the computational domain and mesh. It includes the pulsed jet actuator and a large downstream area in which the pulsed jet develops. The diameter of the actuator is $D = 0.1965\text{m}$. The computational domain is also cylindrical with a diameter of $5D$ and a length of $11D$. The width and length of the slot is $W_s = 2\text{mm}$ and $L_s = 10\text{mm}$, respectively. In this study, the loudspeaker cone is simplified as a diaphragm by keeping the cavity volume approximately unchanged: the diaphragm position does not change the volume of the cavity significantly [25]. This simplification, therefore, provides a close approximation to the experimental conditions. A detailed description of the actuator geometry can be found in Oxlade [26]. The origin of the coordinate system is defined as the centre of the base. The pressure coefficient C_p , Equation (1), is defined as

$$C_p = \frac{p - p_\infty}{\frac{1}{2}\rho U_\infty^2}, \quad (1)$$

where p_∞ is the pressure in the far field, U_∞ is the reference velocity. Following Oxlade et al. [3], U_∞ is defined as 15m/s in this study. The area-weighted averaged pressure coefficient on the base surface, Equation (2), is

$$\langle C_p \rangle = \frac{1}{A_b} \int_\phi \int_r C_p(r, \phi) r dr d\phi, \tag{2}$$

where A_b is the area of the base. The total pressure coefficient, Equation (3), is defined as

$$C_{pT} = \frac{p_T - p_\infty}{\frac{1}{2} \rho U_\infty^2}, \tag{3}$$

where p_T is the total pressure. The pressure coefficient C_p and the velocity components $(\hat{u}, \hat{v}, \hat{w})$ are further decomposed into the time averaged component $\overline{C_p}$, (U, V, W) and the turbulent component C'_p , (u, v, w) with Equation (4):

$$\begin{aligned} C_p &= \overline{C_p} + \tilde{C}_p + C'_p, \\ (\hat{u}, \hat{v}, \hat{w}) &= (U, V, W) + (u, v, w). \end{aligned} \tag{4}$$

The pulsed jet velocity is expressed as a blowing coefficient, Equation (5), which is given by

$$C_\mu = \frac{u_f^2 A_j}{U_\infty^2 A_b}, \tag{5}$$

where u_f is the amplitude of the pulsed jet, defined as the amplitude of the Fourier component of the jet centre line velocity, and A_j is the area of the slot.

The open-source code OpenFOAM is used for the present numerical study. A three-dimensional transient solver based on the PIMPLE algorithm is used to solve compressible Navier-Stokes equations, Equation (6), given by

$$\frac{\partial (\rho \mathbf{u})}{\partial t} + \nabla \cdot (\rho \mathbf{u} \mathbf{u}) = -\nabla p + \nabla \cdot \tau, \tag{6}$$

where \mathbf{u} is the velocity vector, τ is the stress tensor. The PIMPLE algorithm combines the PISO (Pressure Implicit with Splitting of Operator) and SIMPLE (Semi-Implicit Method for Pressure-Linked Equations), with the advantage of reduced Courant number restriction. LES is performed with the standard Smagorinsky subgrid model, which has been extensively verified by Krajnović and Fernandes [12] and Parkin et al. [13]. The numerical scheme is second-order in time discretion. A first/second-order linear-upwind discretisation is used for space terms. The velocity boundary of the computational domain is defined as a zero-gradient boundary, and a non-reflecting pressure boundary is used to minimise the pressure reflection. A no-slip boundary condition is used for the wall boundary of the actuator. A universal wall function based on Spalding’s law is used to reduce the mesh requirement in the near-wall region, reducing the computational cost. A sparse mesh is used for the far field. In the vicinity of the body and in the wake region, the mesh is refined: specifically, the mesh near the slot is further refined to simulate the pulsed jet. A mesh with a total number of 4.5m nodes is used for the pulsed jet computational domain. Since the velocity varies with phase, an adjustable time interval (keeping the Courant number less than 0.7) is used to save computational time while satisfying the CFL condition. Approximately 1,500 time steps are resolved in every pulsed-jet period.

2.2 Actuator boundary condition

In the current study, the pulsed jet actuator is included in the computational domain. The diaphragm periodically ingests and expels the working fluid through a slot to generate the pulsed jet. The diaphragm boundary condition is prescribed as sinusoidal motion in time and parabolic distribution in space. Mane et al. [27] demonstrate that for piezoelectric diaphragm a parabolic surface approximation is more

Table 1. A summary of the boundary conditions for the main variables

Boundary name	Velocity	Pressure	Temperature
Far-field	Zero gradient	Non-reflectional	Fixed value
Diaphragm	Equation (9) (velocity boundary case) or moving wall (moving boundary case)	Zero gradient	Zero gradient
Wall	Non-slip	Zero gradient	Zero gradient

accurate than a logarithmic one. Hence, taking the diaphragm centre as the coordinate origin moving in the x direction, the time-dependent diaphragm profile, Equation (7), is described by

$$x(y, z, t) = (ay^2 + by + cz^2 + dz + e) \sin(2\pi ft), \quad (7)$$

where a, b, c, d, e are constants. For an axisymmetric surface with the maximum displacement in the centre and zero displacement at the edge, the constants $c = a, b = d = 0$, and $e = -\frac{1}{4}aD_d^2$, where D_d is the diameter of the diaphragm. Thus, Equation (7) becomes Equation (8)

$$x(y, z, t) = \left(ay^2 + az^2 - \frac{1}{4}aD_d^2 \right) \sin(2\pi ft). \quad (8)$$

The velocity profile, Equation (9), is achieved by taking the time derivative of Equation (8):

$$\hat{u}_d(y, z, t) = \left(ay^2 + az^2 - \frac{1}{4}aD_d^2 \right) 2\pi f \cos(2\pi ft). \quad (9)$$

The remaining unknown constant, a , is estimated assuming mass conservation with the incompressible flow. Then, since the solver is compressible, an iterative calculation is conducted with a coarse mesh to modify this number to match the pressure or velocity in the corresponding experiment.

The boundary conditions for the computational domain (Fig. 1(a)) can be summarised in Table 1. For the far-field, a zero-gradient boundary is used for the velocity and a non-reflectional boundary condition is used for the pressure. For the diaphragm boundary, as described above, a time-dependent parabolic velocity profile or moving mesh is used. The non-slip wall boundary condition is applied to the boundaries except the diaphragm and the far-field, including the actuator wall, the base and the stationary geometry inside the actuator, etc.

3.0 Boundary condition validation

In this section, the moving boundary condition and the velocity boundary condition are compared based on the round pulsed jet actuator studied experimentally by Feero et al. [24]. The configuration investigated is $f/f_H = 1.07$ (f_H is the Helmholtz resonance frequency), $\bar{p}_c = 160\text{Pa}$ (\bar{p}_c is the cavity pressure). The boundary condition of the diaphragm is iterated to match the cavity pressure. The jet profile on the orifice outlet plane is chosen as the criterion for validation.

Initially, 30 periods are calculated to achieve a stable result, after which another 30 periods are calculated to provide a phase-locked average. The numerical and experimental velocity magnitude distribution near the orifice outlet plane at $x/D_o = 0.075$ (D_o is the diameter of the orifice) is normalised by the maximum centre-line velocity, illustrated in Fig. 2. As noted by Feero et al. [24], and Mu et al. [28], the hot-wire measurements in the experiment do not resolve reverse flow well, leading to uncertainty at the ends of the nozzle ($y/D_o = \pm 0.5$). Therefore, the comparison between the numerical results and the experimental ones is focused on $-0.45 \leq y/D_o \leq 0.45$. This figure shows that the phase-locked average of the velocity distributions is identical for the two boundary conditions. Both results show a qualitatively good agreement with the experimental ones by Feero et al. [24], especially in the suction phase. There is only a small difference near the orifice edge in the blowing phase.

The flow structures identified by the Q -criterion ($Q > 0$) from both the moving boundary and the velocity boundary are shown in Fig. 3. The streamwise velocity is normalised by its maximum and

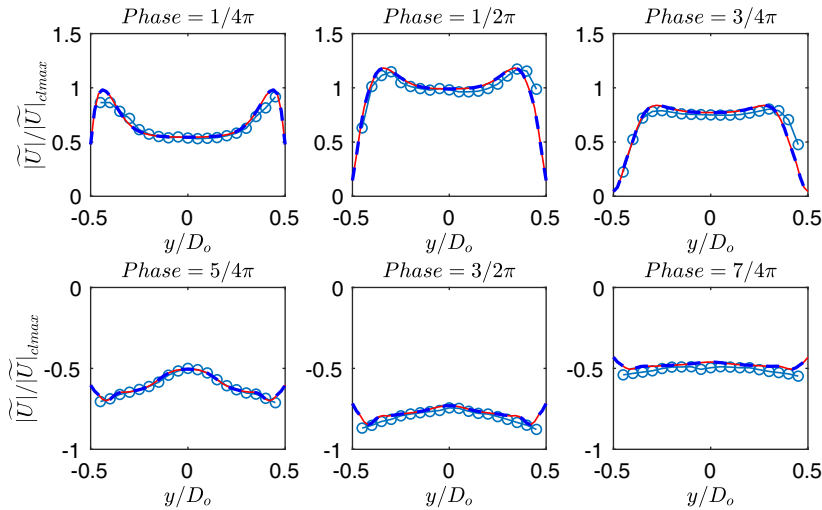


Figure 2. Spatial distribution of normalised velocity magnitude near the orifice outlet plane over six phases. —, Moving boundary. --, Velocity boundary. -o-, Experimental result by Feero et al. [24].

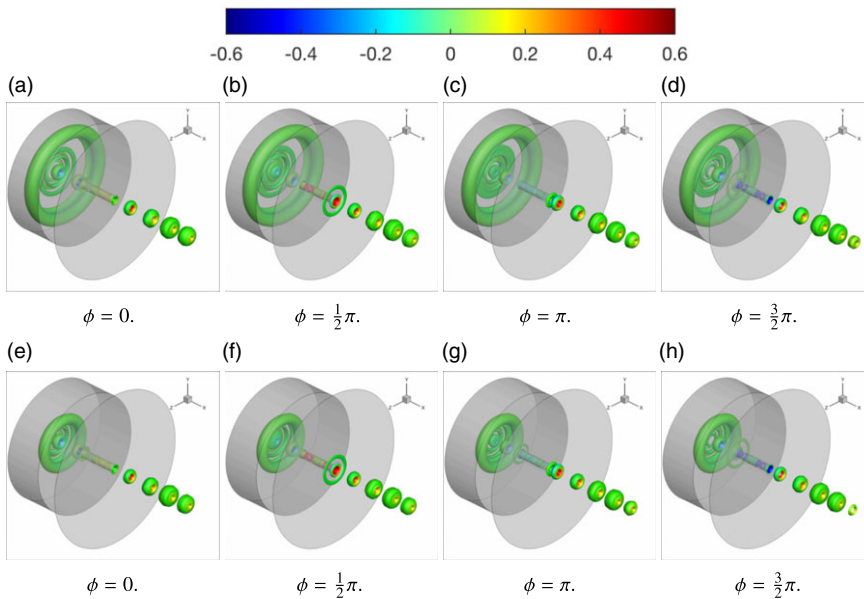


Figure 3. Q -criterion iso-surface contoured by normalised streamwise velocity \hat{u}/\hat{u}_{max} (contour range: $-0.6 \leq \hat{u}/\hat{u}_{max} \leq 0.6$) at $\phi = 0, 1/2\pi, \pi, 3/2\pi$. (a–d) Moving boundary condition. (e–h) Velocity boundary condition. The transparent grey area shows the wall boundary of the actuator. For more details of the actuator geometry, see Feero et al. [24].

imposed on the iso-surface of Q -criterion. These figures illustrate that the vorticity structure produced by these two methods is almost identical in the downstream region outside the actuator. The coherent structure inside the cavity, however, shows significant differences. By comparing Fig. 3(a)–(d) with Fig. 3(e)–(h), it is clear that with the velocity boundary, the flow structure inside the cavity is weaker and smaller than that achieved by the moving boundary condition. In the moving boundary condition, the diaphragm boundary is a moving wall boundary, which is the same as the piezoelectric diaphragm motion, while the velocity boundary condition uses a velocity inlet/outlet boundary to approximate such

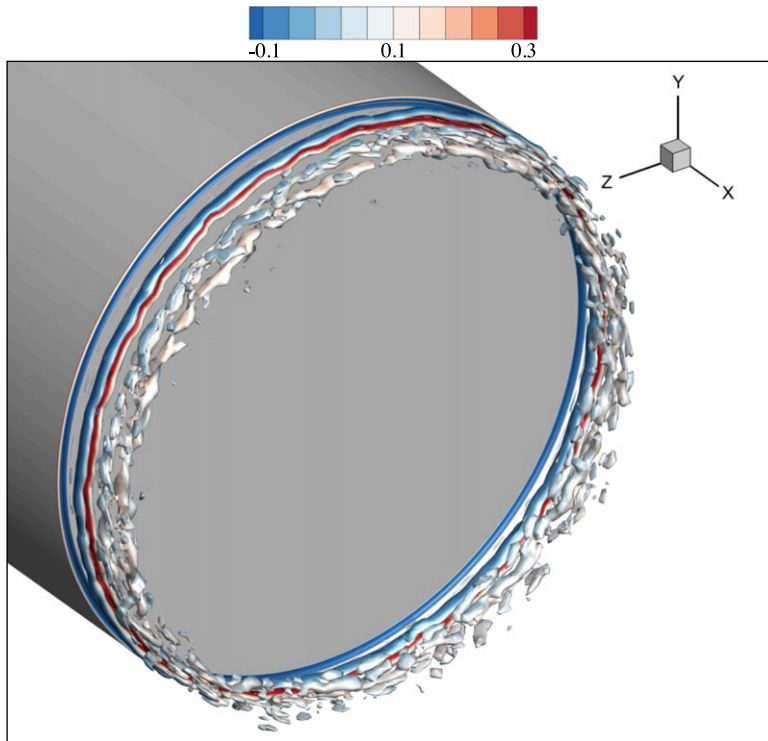


Figure 4. A whole orthographic view of the Q criterion iso-surface contoured by normalised streamwise velocity (contour range: $-0.1 \leq \hat{u}/\hat{u}_{max} \leq 0.3$).

motion. Therefore, with the velocity boundary condition, a considerable portion of the flow is sucked into the diaphragm instead of being reflected. Hence, inside the cavity, the velocity boundary result is probably less accurate than the moving boundary result.

The computational cost of the moving boundary condition is compared with the velocity boundary condition by assessing the computational time with the same computational resource and numerical settings. Since mesh deformation is performed at every iteration in the moving boundary method, to complete the same computation the computational time with the moving boundary condition t_m compared to that with the velocity boundary condition t_v is about $t_m/t_v \approx 250\%$. In conclusion, when the downstream interaction between the pulsed jet with the outer fluid is of interest, the velocity boundary condition can achieve very similar results compared to the moving boundary condition but with a lower computational cost. Conversely, if the fluid motion inside the cavity is important, the moving boundary condition should be used.

4.0 Characteristics of the pulsed jet actuator

In the following sections, the pulsed jet actuator for control of the bluff body wake is studied with the velocity boundary condition, since it requires less computational cost and the analysis is focused on the area away from the diaphragm. The pulsed jet frequency is $f = 200$ Hz, the Strouhal number based on the boundary layer momentum thickness $\theta = 2.14$ mm [3] is $St_\theta = 0.029$, and the pulsed jet velocity coefficient at the slot outlet is $C_\mu = 0.034$.

The pulsed jet structures generated by the actuator are identified with the Q -criterion and illustrated in Fig. 4. It shows that the actuator generates a series of counter-rotating vorticity rings moving downstream, which confirms that the pulsed jet structures observed experimentally in the 2D PIV plane by

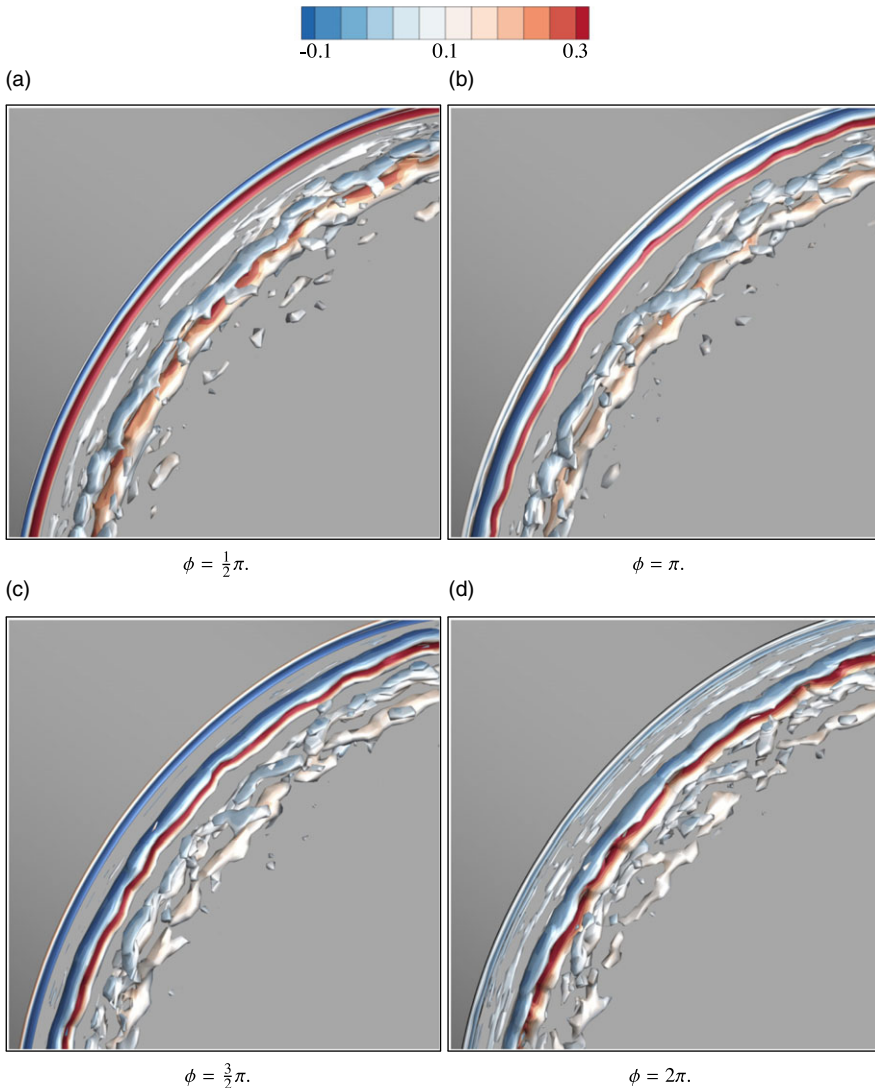


Figure 5. Amplified view of the Q criterion iso-surface contoured by the normalised streamwise velocity at $\phi = \frac{1}{2}\pi, \pi, \frac{3}{2}\pi, 2\pi$ (contour range: $-0.1 \leq \hat{u}/\hat{u}_{max} \leq 0.3$).

Oxlade et al. [3] are in the form of rings. Tracing the pulsed jet generated near the slot edge (Fig. 5), in the initial stage ($\phi = \frac{1}{2}\pi$), the pulsed jet remains coherent as a pair of rings in the vicinity of the inner and outer edges of the slot. The spanwise variation of the jet structure is weak, thus the jet is quasi-two-dimensional. As these vorticity rings propagate downstream ($\phi = \pi \sim 2\pi$), the perturbation in the azimuthal direction grows, which leads the vorticity ring to gradually break up into three-dimensional structures. After $\phi = 2\pi$, the separated vorticity rings rapidly decay, breaking down into small-scale turbulence and eventually dissipating. From their generation near the slot edge, the pulsed jet rings lose coherence after about two periods.

A typical history of the normalised cavity pressure C_p/C_{pmax} , the diaphragm velocity \hat{u}_d/\hat{u}_{dmax} , and the streamwise velocity on the slot outlet plane \hat{u}/\hat{u}_{max} is in Fig. 6. It shows that the phase of the cavity pressure fluctuation is about $\frac{2}{3}\pi$ ahead of the pulsed jet and the diaphragm velocity. This is a physical phenomenon because the pressure gradient is a prerequisite for the formation of the pulsed jet [1]. The

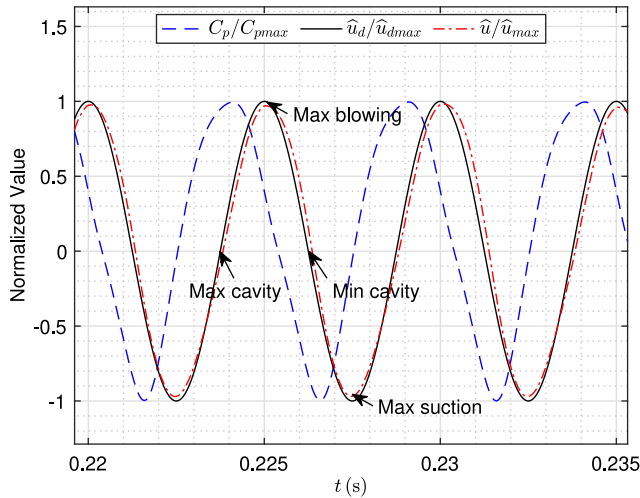


Figure 6. A typical history of the normalised cavity pressure C_p/C_{pmax} , the normalised diaphragm motion velocity \hat{u}_d/\hat{u}_{dmax} and the normalised streamwise velocity \hat{u}/\hat{u}_{max} on the slot outlet plane.

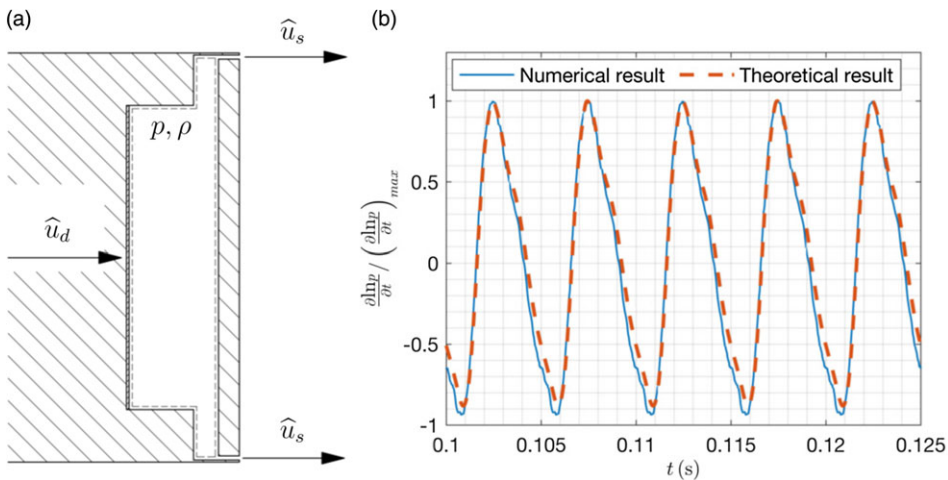


Figure 7. (a) A schematic of the CV bounded by the CS (dashed line). (b) Comparison of the numerical result with the theoretical one calculated using Equation (13).

diaphragm velocity indicates the cavity size: positive \hat{u}_d/\hat{u}_{dmax} means that the diaphragm is compressing the cavity, thus when the positive \hat{u}_d/\hat{u}_{dmax} comes to an end in the time series, the cavity size is minimum; in turn, negative \hat{u}_d/\hat{u}_{dmax} indicates that the cavity is expanding. By correlating the pressure fluctuation to the diaphragm motion, it is evident that the maximum pressure appears when the cavity size is close to the maximum, while the minimum pressure appears when the cavity size is near a minimum. A theoretical analysis is conducted to analyse the cavity pressure phase.

Taking the cavity as a control volume (CV) bounded by the control surfaces (CS), which includes the diaphragm, the slot inlet, and the cavity wall (Fig. 7(a)), the conservation of mass, Equation (10), can be written as

$$\int_{CV} \frac{\partial \rho}{\partial t} dV + \int_{CS} \rho (\mathbf{U} \cdot \mathbf{n}) dA = 0, \tag{10}$$

where \mathcal{V} is the volume of the control volume, A is the area of the control surface. Since the pressure fluctuation propagates with the speed of sound, we assume that in the CV, the pressure and the density are spatially uniform but change in time, thus Equation (10) becomes Equation (11),

$$\frac{\partial \rho}{\partial t} \mathcal{V} + \rho \int_{CS_s} \hat{u}_s dA - \rho \int_{CS_d} \hat{u}_d dA = 0, \tag{11}$$

where \hat{u}_s is the streamwise velocity of the pulsed jet, \hat{u}_d is the streamwise velocity of the diaphragm, d denotes diaphragm, and s denotes the slot. Rearranging this equation to get Equation (12),

$$\frac{1}{\rho} \frac{\partial \rho}{\partial t} \mathcal{V} = \frac{\partial \ln \rho}{\partial t} \mathcal{V} = \int_{CS_d} \hat{u}_d dA - \int_{CS_s} \hat{u}_s dA. \tag{12}$$

With the assumption of the ideal gas law, $\rho = p/RT$, and constant temperature, we obtain Equation (13),

$$\frac{\partial \ln p}{\partial t} \propto \frac{1}{\mathcal{V}} \left(\int_{CS_d} \hat{u}_d dA - \int_{CS_s} \hat{u}_s dA \right). \tag{13}$$

To validate the model given by Equation (13), the theoretical result is compared to the numerical one with phase-locked averages. The theoretical estimate of $\partial \ln p / \partial t$ is computed by calculating the right-hand side of the equation with the streamwise diaphragm velocity u_d , the streamwise velocity at the inlet of the slot u_s and the cavity volume \mathcal{V} . The numerical estimate of $\partial \ln p / \partial t$ is obtained directly. Figure 7(b) shows that the model is able to represent the phase change of the pressure well. The normalised magnitude of the pressure gradient $\partial \ln p / \partial t$ also shows good agreement.

The model takes the difference between axial mass flux at the diaphragm and that at the slot inlet, so it clarifies whether the flow can be adequately described by temporal changes with a spatially averaged velocity alone. Practically, then one could use a harmonically varying, parabolic-shaped diaphragm at the inlet, and measured velocity at the slot to compare to simulation data. Equation (13) shows that the phase of the cavity pressure is determined by time integration of the pulsed jet and the diaphragm motion. The domain from the diaphragm face to the external flow supports a spatially evolving pressure wave that predominantly propagates downstream, and ignores any pressure reflections inside the cavity. Pressure changes downstream of the slot can also propagate upstream to the diaphragm since the flow inside the slot is subsonic. The pressure propagating downstream manifests as a pressure wave which causes a large pressure fluctuation on the base.

Figure 8(a) shows the time-averaged total pressure distribution on a plane near the slot. This figure shows that the total pressure loss is concentrated in the vicinity of the sharp slot edge which leads to flow separation. The total pressure loss inside the cavity is relatively small since the flow velocity is low there. Loss in total pressure from diaphragm to slot outlet is due to static pressure drop not recovered by an increase in velocity. A time series of the total pressure coefficient at the slot inlet $\langle C_{pTi} \rangle$ at $x/L_s = -1$, the slot outlet $\langle C_{pTo} \rangle$ at $x/L_s = 0$ and the difference between the inlet and the outlet $\langle C_{pTi} - C_{pTo} \rangle$ is shown on Fig. 8(c). In the constant blowing jet, the total pressure near the slot inlet is higher than that near the slot outlet, while in the pulsed jet the periodic change of the cavity pressure and jet direction results in total pressure variation. Thus, depending on the phase of the pulsed jet, the jet direction can be from the slot inlet to the outlet or reverses, and the total pressure in the slot inlet can be either higher or lower than the outlet.

The mean total pressure coefficient variation inside the slot is plotted in Fig. 8(d). Since the pulsed jet is characterised by periodic changes in the jet direction and cavity pressure, the mean total pressure coefficient is not constantly decreasing towards the outside. However, it is still clear that the total pressure coefficient dramatically decreases near the slot edge, i.e., at near $x/L_s = -1$ and $x/L_s = 0$. To reduce the total pressure loss through the slot, a round edge is applied to the slot. Figure 8(b) and (d) show that the total pressure loss in the round edge slot is lower than that in the sharp edge slot. By using a round edge, the total pressure coefficient in the middle of the slot ($x/L_s = -0.5$) is increased from $\langle C_{pT} \rangle = 0.02$ to $\langle C_{pT} \rangle = 0.05$. However, since the vortex rings generated by a round edge is weaker than that generated by the sharp edge, it is likely to provide a reduced influence on the wake.

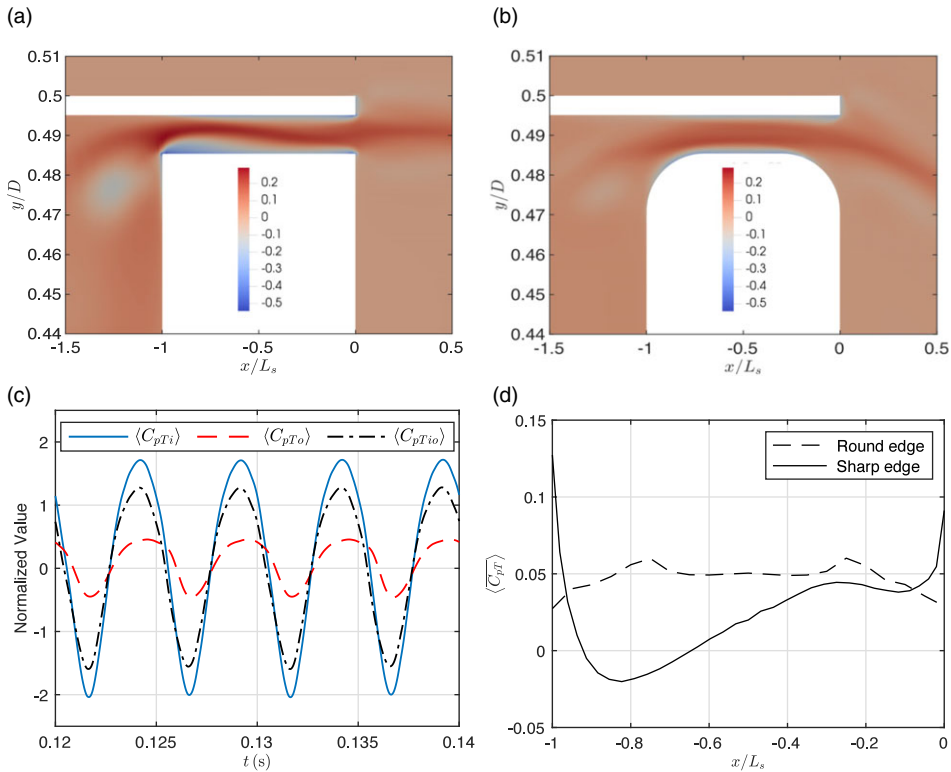


Figure 8. The mean total pressure $\overline{C_{pT}}$ distribution in the vicinity of the slot for (a) the sharp edge slot and (b) the round edge slot. (c) A time series of the area-weighted averaged total pressure coefficient at the slot inlet $\langle C_{pTi} \rangle$, the slot outlet $\langle C_{pTo} \rangle$, and the difference between the inlet and the outlet $\langle C_{pTi0} \rangle$ for the slot with a sharp edge. (d) Area-weighted averaged mean total pressure coefficient $\langle C_{pT} \rangle$ along the slot. $x/L_s = 0$ is the outlet of the slot, and $x/L_s = -1$ is the entry of the slot.

5.0 Dynamic mode decomposition of pressure field

In this section, DMD [29] is applied to study the pressure field downstream of the actuator and on the actuator base. DMD is a data-based equation-free decomposition method to extract the dominating mode of a dynamic system. It is able to extract low-rank physically interpretable flow features of a high-dimensional field according to their frequency. In the present work, following the exact DMD algorithm described by Kutz et al. [30], the DMD modes of the pressure field in the range $0 \leq x/D \leq 10$, $-2.5 \leq y/D \leq 2.5$ have been decomposed without excluding the long-time mean. The number of sampling points in the spatial coordinate is 400×200 . The temporal coordinate, each period ($TU_\infty/D = 0.38$) is sampled with 100 snapshots. A total number of five periods are sampled to conduct the decomposition. With the DMD modes ϕ , the approximate state of the dynamic system $x(t)$ can be reconstructed by Equation (14),

$$x(t) \approx \sum_{k=1}^N \phi_k \exp(\omega_k t) a_k, \tag{14}$$

where $\omega_k = \log(\lambda_k) / \Delta t$, λ is the DMD eigenvalue. The growth rate σ is defined as $\sigma = Re(\omega)$, indicating whether the corresponding modes are growing, decaying or stable. The oscillation frequency of the DMD modes f is defined as $f = |Im(\omega) / 2\pi|$. Following Schmid et al. [31], the amplitude of each DMD mode $|a_k|$ is achieved by projecting the data sequence on the identified dynamic modes. Assembling the multiple data sequences into matrix form X , the Equation (14) can be rewritten as Equation (15),

Table 2. Summary of the first four dominant DMD modes

Mode	λ	σ	f (Hz)
1	$0.9980 + 0.0628i$	0.0018	200
2	$0.9921 + 0.1254i$	-0.5525	400
3	$0.9822 + 0.1874i$	-0.8796	600
4	$0.9685 + 0.2486i$	-1.4690	800

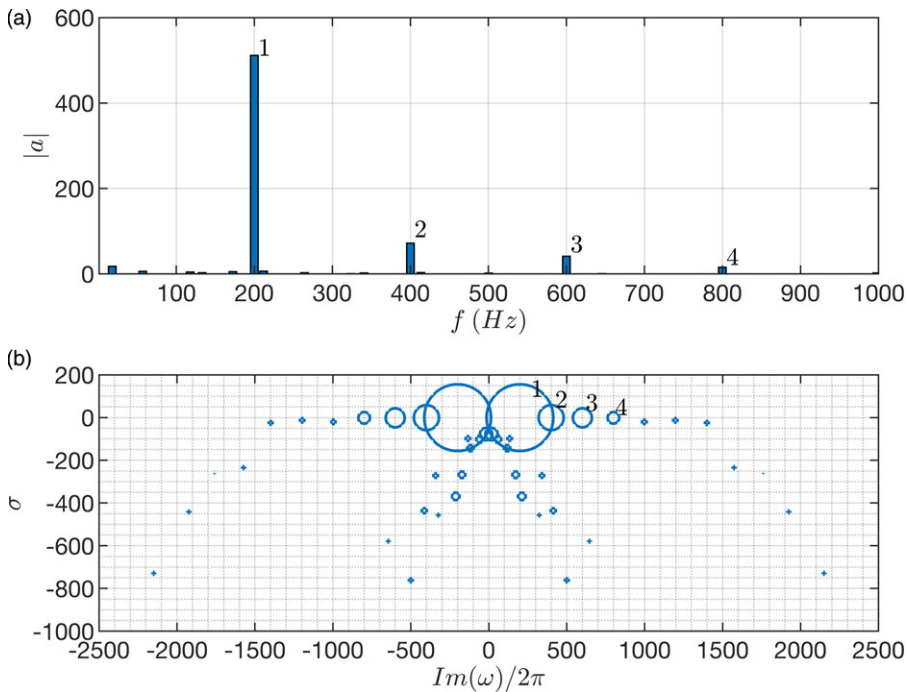


Figure 9. DMD spectrum of the actuator pressure field in the downstream. (a) The amplitude $|a|$ of each DMD mode against frequency. (b) The growth rate σ of each DMD mode, the size of the cycle indicating the amplitude of the mode.

$$\underbrace{\begin{bmatrix} | & | & \dots \\ x_1 & x_2 & \dots \\ | & | & \dots \end{bmatrix}}_X \approx \underbrace{\begin{bmatrix} | & | & \dots \\ \phi_1 & \phi_2 & \dots \\ | & | & \dots \end{bmatrix}}_\Phi \underbrace{\begin{bmatrix} a_1 & 0 & \dots \\ 0 & a_2 & \dots \\ \vdots & \vdots & \ddots \end{bmatrix}}_a \underbrace{\begin{bmatrix} 1 & \lambda_1 & \dots & \lambda_1^{m-2} \\ 1 & \lambda_2 & \dots & \lambda_2^{m-2} \\ \vdots & \vdots & \ddots & \vdots \end{bmatrix}}_{V_{and}}. \tag{15}$$

Figure 9(a) shows the amplitude of the DMD modes against the corresponding frequency. The mean mode is omitted. Four DMD modes dominate the pressure field, each one corresponding to $f = 200\text{Hz}$, 400Hz , 600Hz and 800Hz . Detailed information can be found in Table 2. Since negative frequency is unphysical, $Im(\omega)/2\pi$ is used as x coordinate to illustrate the full map of the growth rate σ (Fig. 9(b)). The first four dominating DMD modes are located in the close vicinity of the $\sigma = 0$ axis. The detailed growth rate (see Table 2) indicates that these DMD modes are stabilised without growing or decaying. Since the pressure wave is generated periodically, the peak magnitude between two successive waves is neither growing or decaying.

The first three modes are illustrated in Fig. 10. The first is characterised by a pair of high-amplitude regions in the vicinity of the slot and a large wave downstream. The other two DMD modes show that

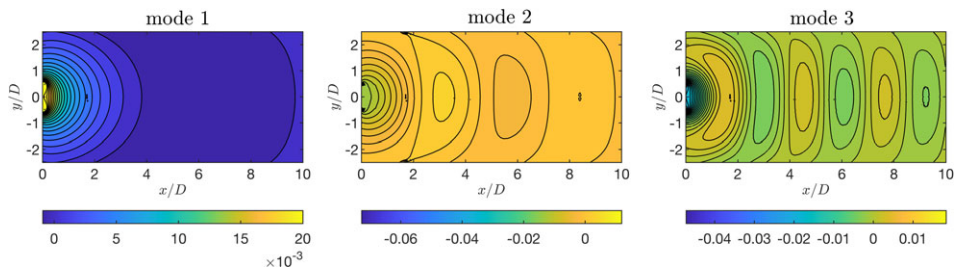


Figure 10. Visualisation of the first three DMD modes in the downstream region.

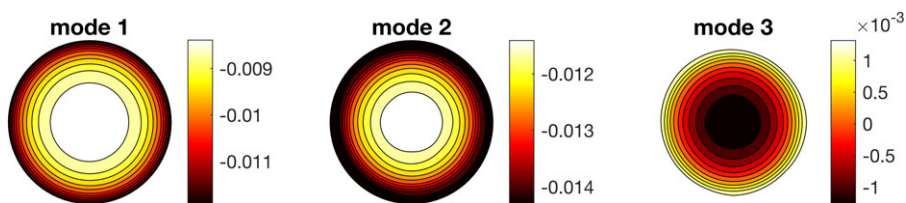


Figure 11. Visualisation of the first three DMD modes on the actuator base.

downstream a series of high-frequency small-scaled harmonic structures exist. The oscillation frequency of these structures is several times higher than the first mode.

The time-resolved pressure data on the base is collected from 64 equispaced probe locations described by Rigas et al. [32] to analyse the structure of the pressure wave on the base. Since the spatial resolution is significantly lower than the temporal resolution, an augmented matrix obtained by stacking the state multiple times is used to perform DMD [33, 34]. The amplitude map and the growth map are identical to that of the downstream DMD (Table 2) and therefore is not displayed. The first three base DMD modes, which oscillate at frequency $f = 200\text{Hz}$, 400Hz , and 600Hz respectively, are displayed in Fig. 11. These modes are axisymmetric since the pressure wave generated by the axisymmetric actuator is axisymmetric.

6.0 Conclusions

Numerical simulation of the pulsed jet actuator is conducted with a 3D compressible LES simulation. An analysis is performed to study the effects of boundary conditions for the pulsed jet and its pressure characteristics. The cavity pressure, the total pressure loss in the slot and the downstream pressure field are analysed using a theoretical model, total pressure fields and DMD, respectively. The pulsed jet is driven at $f = 200\text{Hz}$ ($St_\theta = 0.029$) and $C_\mu = 0.034$.

Validation of the boundary condition shows that in the vicinity of the slot and in the downstream region the velocity boundary condition is able to achieve almost identical results as the moving boundary condition but at a lower computational cost. Both results agree well with the corresponding experimental result by Feero et al. [24]. However, inside the cavity, the cavity flow reflection from the diaphragm is stronger with the moving boundary condition than that with the velocity boundary condition. Therefore, when studying the pulsed jet outside the cavity or downstream, the velocity boundary condition can be used at a lower computational cost. When simulating the flow structures inside the cavity, the moving boundary condition will probably lead to more reliable results.

The result of the pulsed jet shows that the periodic motion of the diaphragm generates pressure waves which cause significant pressure fluctuations on the actuator base. An analysis of the cavity pressure phase lag shows that it is determined by the time integration of the pulsed jet and the diaphragm motion.

The mean total pressure distribution shows that the total pressure loss is concentrated in the vicinity of the slot edge where there is strong separation at sharp edges. Total pressure loss is reduced with rounded edges, increasing the total pressure coefficient in the middle of the slot ($x/L_s = -0.5$) from $\overline{\langle C_{pT} \rangle} = 0.02$ to $\overline{\langle C_{pT} \rangle} = 0.05$, while a sharp edge is more efficient at generating pulsed jet vorticity. The downstream pressure field of the actuator is analysed with the DMD, which is used to extract coherent structures oscillating with the same frequency as the diaphragm motion. Meanwhile, it shows that some small-scaled high-frequency substructures exist. The pressure wave on the base is analysed by DMD, showing that the DMD modes of the pressure wave are axisymmetric.

References

- [1] Glezer, A. and Amitay, M. Synthetic jets, *Ann. Rev. Fluid Mech.*, 2002, **34**, pp 503–529.
- [2] Smith, B.L. and Glezer, A. Jet vectoring using synthetic jets, *J. Fluid Mech.*, 2002, **458**, pp 1–34.
- [3] Oxlade, A.R., Morrison, J.F., Qubain, A. and Rigas, G. High-frequency forcing of a turbulent axisymmetric wake, *J. Fluid Mech.*, 2015, **770**, pp 305–318.
- [4] Rigas, G., Morgans, A.S. and Morrison, J.F. Weakly nonlinear modelling of a forced turbulent axisymmetric wake, *J. Fluid Mech.*, 2017, **814**, pp 570–591.
- [5] Cabitza, S. Active Control of the Wake from a Rectangular-Sectioned Body, PhD Thesis, Imperial College London, 2014.
- [6] Barros, D., Borée, J., Noack, B.R., Spohn, A. and Ruiz, T. Bluff body drag manipulation using pulsed jets and Coanda effect, *J. Fluid Mech.*, 2016, **805**, pp 422–459.
- [7] Haffner, Y., Borée, J., Spohn, A. and Castelain, T. Unsteady Coanda effect and drag reduction for a turbulent wake, *J. Fluid Mech.*, 2020, **899**, pp A36.
- [8] Haffner, Y., Castelain, T., Borée, J. and Spohn, A. Manipulation of three-dimensional asymmetries of a turbulent wake for drag reduction, *J. Fluid Mech.*, 2021, **912**, pp A6.
- [9] Pastoor, M., Henning, L., Noack, B.R., King, R. and Tadmor, G. Feedback shear layer control for bluff body drag reduction, *J. Fluid Mech.*, 2008, **608**, pp 161–196.
- [10] Lambert, T.J., Vukasinovic, B. and Glezer, A. Aerodynamic flow control of axisymmetric bluff body by coupled wake interactions, *AIAA J.*, 2018, **56**, pp 2992–3007.
- [11] Lambert, T.J., Vukasinovic, B. and Glezer, A. A freely yawing axisymmetric bluff body controlled by near-wake flow coupling, *J. Fluid Mech.*, 2019, **863**, pp 1123–1156.
- [12] Krajnović, S. and Fernandes, J. Numerical simulation of the flow around a simplified vehicle model with active flow control, *Int. J. Heat Fluid Flow*, 2011, **32**, pp 192–200.
- [13] Parkin, D.J., Thompson, M.C. and Sheridan, J. Numerical analysis of bluff body wakes under periodic open-loop control, *J. Fluid Mech.*, 2014, **739**, pp 94–123.
- [14] Dahan, J.A., Morgans, A.S. and Lardeau, S. Feedback control for form-drag reduction on a bluff body with a blunt trailing edge, *J. Fluid Mech.*, 2012, **704**, pp 360–387.
- [15] Kang, S. and Choi, H. Suboptimal feedback control of turbulent flow over a backward-facing step, *J. Fluid Mech.*, 2002, **463**, pp 201–227.
- [16] Rumsey, C., Gatski, T., Sellers, W., Vatsa, V. and Viken, S. Summary of the 2004 CFD validation workshop on synthetic jets and turbulent separation control, 2nd AIAA Flow Control Conference, 2004, p 2217.
- [17] Rizzetta, D.P., Visbal, M.R. and Stanek, M.J. Numerical investigation of synthetic-jet flowfields, *AIAA J.*, 1999, **37**, pp 919–927.
- [18] Yoo, I., Lee, S., Kim, W. and Kim, C. Boundary condition models for synthetic jet simulation, 48th AIAA Aerospace Sciences Meeting Including the New Horizons Forum and Aerospace Exposition, 2010, p 1413.
- [19] Jain, M., Puranik, B. and Agrawal, A. A numerical investigation of effects of cavity and orifice parameters on the characteristics of a synthetic jet flow, *Sens. Actuators A Phys.*, 2011, **165**, pp 351–366.
- [20] Bazdidi-Tehrani, F., Abouata, A., Hatami, M. and Bohlooli, N. Investigation of effects of compressibility, geometric and flow parameters on the simulation of a synthetic jet behaviour, *Aeronaut J.*, 2016, **120**, pp 521–546.
- [21] Ma, X., Guo, H., Fan, Z. and Zhang, L. Investigating of simulation methods for synthetic jet, *Procedia Eng.*, 2012, **31**, pp 416–421.
- [22] Liu, Q., Kazakidi, A., Medeiros, M.A. and Theofilis, V. Numerical simulation of a synthetic jet with OpenFOAM, in *Instability and Control of Massively Separated Flows*, 2015, **52**, pp 197–202.
- [23] Zhu, T. and Morrison, J.F. Simulation of the turbulent axisymmetric bluff body wake with pulsed jet forcing, *Phys. Rev. Fluids*, 2021, **6**, p 124604.
- [24] Feero, M.A., Lavoie, P. and Sullivan, P.E. Influence of cavity shape on synthetic jet performance, *Sens. Actuators A Phys.*, 2015, **223**, pp 1–10.
- [25] Utturkar, Y., Mittal, R., Rampunggoon, P. and Cattafesta, L. Sensitivity of synthetic jets to the design of the jet cavity, 40th AIAA Aerospace Sciences Meeting & Exhibit, 2002, p 124.
- [26] Oxlade, A. High-Frequency Pulsed Jet Forcing of an Axisymmetric Bluff Body Wake, PhD thesis, Imperial College London, 2013.

- [27] Mane, P., Mossi, K., Rostami, A., Bryant, R. and Castro, N. Piezoelectric actuators as synthetic jets: cavity dimension effects, *J. Intel. Mater. Syst. Struct.*, 2007, **18**, pp 1175–1190.
- [28] Mu, H., Yan, Q., Wei, W. and Sullivan, P.E. Synthetic jet performance for different axisymmetric cavities analyzed with three-dimensional lattice-boltzmann method, *AIAA J.*, 2018, **56**, pp 1–7.
- [29] Schmid, P.J. Dynamic mode decomposition of numerical and experimental data, *J. Fluid Mech.*, 2010, **656**, pp 5–28.
- [30] Kutz, J.N., Fu, X. and Brunton, S.L. Multiresolution dynamic mode decomposition, *SIAM J. Appl. Dyn. Syst.*, 2016, **15**, pp 713–735.
- [31] Schmid, P.J., Violato, D. and Scarano, F. Decomposition of time-resolved tomographic PIV, *Exp. Fluids*, 2012, **52**, pp 1567–1579.
- [32] Rigas, G., Oxlade, A.R., Morgans, A.S. and Morrison, J.F. Low-dimensional dynamics of a turbulent axisymmetric wakes, *J. Fluid Mech.*, 2014, **755**, p R5.
- [33] Tu, J.H., Rowley, C.W., Luchtenburg, D.M., Brunton, S.L. and Kutz, J.N. On dynamic mode decomposition: theory and applications, *J. Comput. Dyn.*, 2014, **1**, pp 391–421.
- [34] Brunton, B.W., Johnson, L.A., Ojemann, J.G. and Kutz, J.N. Extracting spatial-temporal coherent patterns in large-scale neural recordings using dynamic mode decomposition, *J. Neurosci. Methods*, 2016, **258**, pp 1–15.